SENSOR AND SIMULATION NOTES

Note 323

April 1990

THE EXTERNAL ENVIRONMENT OF VPD-II:

SPACE-WAVE FIELD

Kendall F. Casey
JAYCOR
39650 Liberty Street, Suite 320
Fremont, CA 94538

Abstract

The far-zone field radiated by the VPD-II EMP environment simulator is calculated. The frequency-domain field is obtained from the assumed spatial variation of the antenna surface current density, which is determined by the nonuniform resistive loading. Equivalent circuits for the Marx generator and for the antenna itself are used to determine the current at the feed point of the antenna. Numerical results are presented which show the effect of the wire-mesh ground plane on the radiated field. It is found that both the peak amplitude and the rise rate of the time-domain radiated field increase as the observation angle increases to around 65°. When the mesh ground plane is present, these quantities remain nearly constant up to observer angles very close to 90°; the peak electric-field amplitude at a distance of one kilometer from the simulator is approximately 3 kV/m for an observer well above the air-ground interface. When the ground plane is absent, the peak amplitude and rise rate decrease rapidly as the observation angle is increased beyond 65°; the peak electric-field amplitude at a distance of one kilometer from the simulator is approximately 2.25 kV/m.

1 Introductory Remarks

The Vertically Polarized Dipole EMP simulator known as VPD-II and located at Kirtland AFB in New Mexico was designed to produce an electromagnetic field in its working volume (close to the air-ground interface) which is similar to that associated with the high-altitude nuclear electromagnetic pulse (EMP). The peak electric field produced by VPD-II at the center of the test pad (100 meters from the apex of the simulator) is approximately 35 kV/m; the 10%-90% rise time of the field is less than 10 ns. Our purpose in this note is to formulate an analytical model from which the electromagnetic field radiated by VPD-II can be calculated over a wide range of observation angles and distances. Existing field models [1] account well for the field near the air-ground interface in the working volume but may not adequately describe the field at higher elevation angles or longer ranges.

Our interest in this problem results from the need to understand the external electromagnetic environment created by this and other EMP environment simulators. By "external", we mean the region well outside the working volume. The radiated-field or space-wave part of this external environment is dominant at observer locations far from the simulator and well above the air-ground interface, and is of particular interest for reasons of aircraft safety. The ground-wave environment is dominant for observers near the air-ground interface and will be considered in a separate note.

The electromagnetic design of the VPD-II EMP environment simulator is discussed in [2]. Differences between VPD-II and its predecessor, known as ACHILLES I or VPD-I, are reviewed in [3]. Some early calculations of the field

2

environment at locations relatively remote from the working volume are presented in [4], based on the theoretical development in [1]; field mapping of the completed simulator is discussed in [5]. Related studies of conical antennas over a perfect ground are described in [6] and [7]. We remark that the EMPRESS-II EMP environment simulator operated by the Navy is similar in design to VPD-II. The analysis described in this note than therefore be applied to the determination of the external environment of that simulator.

In the next section we develop an expression for the far-zone radiated field of the VPD-II antenna. We use the spatial variation of the surface current density established by the resistive loading on the antenna to evaluate the vector potential and, from that, the electric field. In Section 3 we determine the antenna feed current from equivalent circuits for the Marx generator and the antenna itself. Representative numerical results for the radiated field are presented in Section 4. Section 5 concludes the note. Details of the asymptotic high-frequency analysis of the radiated field are given in the Appendix.

2 Antenna Model and Radiated Field

The VPD-II facility is shown in Figure 1. The simulator consists of a multi-megavolt Marx generator located underground beneath the antenna; the antenna itself; a wire-mesh ground plane; command, control, and instrumentation facilities; and a test pad. The antenna is a right circular cone with a top cap. The half-angle of the cone at the ground plane is 40.4°, changing to 42.3° when the cone makes the transition from solid metal to a resistively loaded wire mesh; the transition
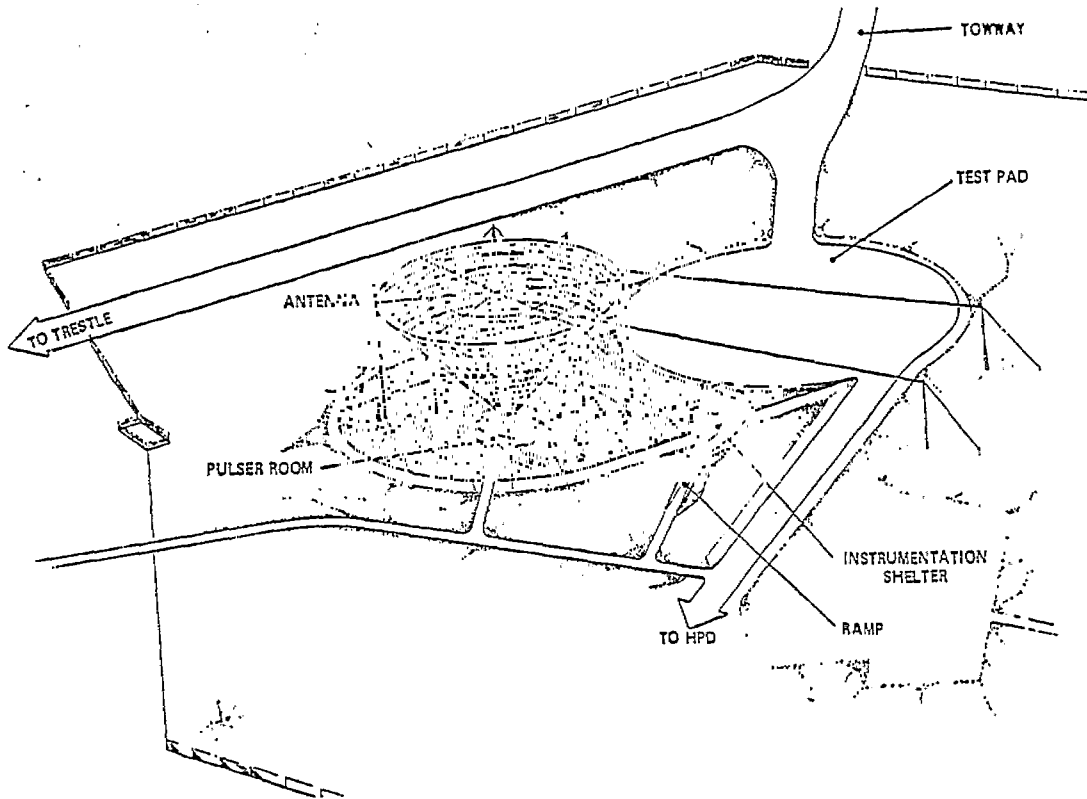
3

Figure 1: The VPD-II EMP simulator facility.

occurs six meters above the ground. The effective electrical half-angle of the cone is 40.4°, yielding a value of 60 ohms for the high-frequency antenna input impedance.

The resistive loading on the antenna [1] was designed to produce a surface current density of the form

$$\vec{J_s}(\vec{r}\,', t) = \frac{I_0(t - r'/c)(1 - r'/r_0)}{2\pi r' \sin\theta_0}\, \vec{a}_{r'} \qquad (0 \le r' \le r_0) \tag{1}$$

where θ_0 denotes the half-angle of the cone, r' is the radial coordinate along the surface of the cone, and $\vec{a}_{r'}$ is the unit vector in the r'-direction. The slant height of the cone is denoted r_0 and is equal to 52.6 m. $I_0(t)$ is the current at the antenna feed point. The vanishing of the surface current density at the top of the cone reduces the contributions to the total electromagnetic field which result from
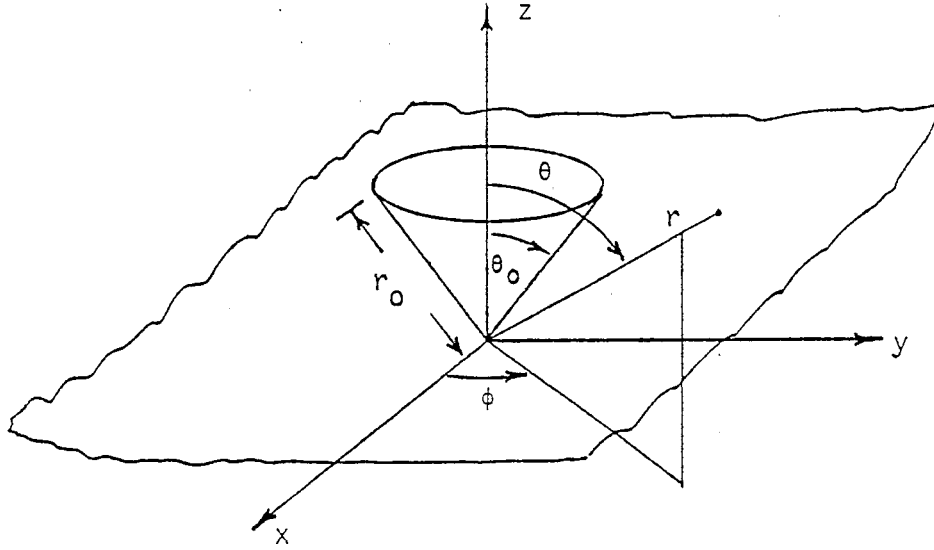
4

Figure 2: Geometry of the model problem. The $z = 0$ plane is initially assumed to be perfectly conducting.

diffraction at the boundary between the cone and the top cap. The surface current density on the top cap of the antenna is small, because of the high resistance at the upper edge of the cone. Its contribution to the radiated field is expected to be small, except perhaps at very late times, and is not considered herein.

We shall initially assume that the ground beneath the antenna is perfectly conducting. The geometry of the modeling problem is shown in Figure 2. It is evident by symmetry that the radiated field is independent of the azimuthal angle ϕ. In the frequency domain (the time dependence $\exp(j\omega t)$ is assumed and suppressed) the surface current density is given by

$$\tilde{\vec{J}}_s\left(\vec{r}\,',j\omega\right) = \frac{\tilde{I}_0(j\omega)(1 - r'/r_0)e^{-jkr'}}{2\pi r' \sin\theta_0}\, \vec{a}_{r'} \quad (0 \leq r' \leq r_0) \tag{2}$$

5

where $\tilde{I}_0(j\omega)$ is the frequency-domain current at the feed point and $k = \omega/c$ denotes the free-space propagation constant; c is the speed of light. The field components established by the antenna currents are $\tilde{E}_\theta, \tilde{E}_r$, and $\tilde{H}_\phi$. In the far zone, the important field components are $\tilde{E}_\theta$ and $\tilde{H}_\phi$; these components are related by

$$\tilde{E}_\theta = Z_0 \tilde{H}_\phi \tag{3}$$

where $Z_0 = 120\pi$ ohms denotes the intrinsic impedance of free space. The far-zone electric field $\tilde{E}_\theta$ is given in terms of the vector potential $\vec{A}$ by

$$\tilde{E}_\theta = -jkZ_0\vec{a}_\theta \cdot \vec{A} \quad (kr \to \infty) \tag{4}$$

where $\vec{a}_\theta$ denotes the unit vector in the θ-direction. The vector potential is given in the far zone by the integral

$$\vec{A} = \frac{\tilde{I}_0(j\omega)e^{-jkr}}{4\pi r} \int_0^{r_0} dr' \frac{1}{2\pi} \int_0^{2\pi} d\phi' \left(1 - \frac{r'}{r_0}\right) e^{-jkr'} \cdot \tag{5}$$

$$\left[\vec{a}_{r'} e^{jkr'\vec{a}_{r'}\cdot\vec{a}_r} - \vec{a}_{r''} e^{jkr'\vec{a}_{r''}\cdot\vec{a}_r}\right] \quad (kr \to \infty)$$

where $\vec{a}_r$ is the unit vector in the r-direction. The vector $r'\vec{a}_{r'}$ is the position vector of a source point on the cone itself; $r'\vec{a}_{r''}$ is the position vector of the corresponding image point in the air-ground interface.

Using eq. (4) and carrying out the integration over r' in eq. (5), we obtain the following expression for $\tilde{E}_\theta$:

$$\tilde{E}_\theta = -\frac{Z_0 \tilde{I}_0(j\omega)}{4\pi r} e^{-jkr} \left(I_1 - \frac{I_2}{jkr_0} + \frac{I_3}{jkr_0} e^{-jkr_0}\right) \tag{6}$$

6

with

$$I_1 = \frac{1}{2\pi} \int_0^{2\pi} d\phi' \left[\frac{\vec{a}_{r'} \cdot \vec{a}_\theta}{1 - \vec{a}_{r'} \cdot \vec{a}_r} - \frac{\vec{a}_{r''} \cdot \vec{a}_\theta}{1 - \vec{a}_{r''} \cdot \vec{a}_r} \right] \tag{7}$$

$$I_2 = \frac{1}{2\pi} \int_0^{2\pi} d\phi' \left[\frac{\vec{a}_{r'} \cdot \vec{a}_\theta}{(1 - \vec{a}_{r'} \cdot \vec{a}_r)^2} - \frac{\vec{a}_{r''} \cdot \vec{a}_\theta}{(1 - \vec{a}_{r''} \cdot \vec{a}_r)^2} \right] \tag{8}$$

$$I_3 = \frac{1}{2\pi} \int_0^{2\pi} d\phi' \left[\frac{\vec{a}_{r'} \cdot \vec{a}_\theta e^{jkr_0 \vec{a}_{r'} \cdot \vec{a}_r}}{(1 - \vec{a}_{r'} \cdot \vec{a}_r)^2} - \frac{\vec{a}_{r''} \cdot \vec{a}_\theta e^{jkr_0 \vec{a}_{r''} \cdot \vec{a}_r}}{(1 - \vec{a}_{r''} \cdot \vec{a}_r)^2} \right] \tag{9}$$

and

$$\vec{a}_{r'} \cdot \vec{a}_r = \cos\theta \cos\theta_0 + \sin\theta \sin\theta_0 \cos(\phi - \phi') \tag{10}$$

$$\vec{a}_{r''} \cdot \vec{a}_r = -\cos\theta \cos\theta_0 + \sin\theta \sin\theta_0 \cos(\phi - \phi') \tag{11}$$

$$\vec{a}_{r'} \cdot \vec{a}_\theta = -\sin\theta \cos\theta_0 + \cos\theta \sin\theta_0 \cos(\phi - \phi') \tag{12}$$

$$\vec{a}_{r''} \cdot \vec{a}_\theta = \sin\theta \cos\theta_0 + \cos\theta \sin\theta_0 \cos(\phi - \phi') \tag{13}$$

We can readily modify these results to account for the presence of an imperfectly conducting ground, since we are working with the far field. The second terms in the integrands for I_1, I_2, and I_3 give the field contributions which arise because of reflection from the plane $z = 0$. We multiply these terms by $R(\theta)$, the reflection

7

coefficient for parallel-polarized plane waves incident at an angle θ on the air-ground interface, obtaining

$$I_1 = \frac{1}{2\pi} \int_0^{2\pi} d\phi' \left[\frac{\vec{a}_{r'} \cdot \vec{a}_\theta}{1 - \vec{a}_{r'} \cdot \vec{a}_r} - \frac{R(\theta)\vec{a}_{r''} \cdot \vec{a}_\theta}{1 - \vec{a}_{r''} \cdot \vec{a}_r} \right] \tag{14}$$

$$I_2 = \frac{1}{2\pi} \int_0^{2\pi} d\phi' \left[\frac{\vec{a}_{r'} \cdot \vec{a}_\theta}{(1 - \vec{a}_{r'} \cdot \vec{a}_r)^2} - \frac{R(\theta)\vec{a}_{r''} \cdot \vec{a}_\theta}{(1 - \vec{a}_{r''} \cdot \vec{a}_r)^2} \right] \tag{15}$$

$$I_3 = \frac{1}{2\pi} \int_0^{2\pi} d\phi' \left[\frac{\vec{a}_{r'} \cdot \vec{a}_\theta e^{jkr_0 \vec{a}_{r'} \cdot \vec{a}_r}}{(1 - \vec{a}_{r'} \cdot \vec{a}_r)^2} - \frac{R(\theta)\vec{a}_{r''} \cdot \vec{a}_\theta e^{jkr_0 \vec{a}_{r''} \cdot \vec{a}_r}}{(1 - \vec{a}_{r''} \cdot \vec{a}_r)^2} \right] \tag{16}$$

We remark that $R(\pi/2) = -1$ for an imperfectly conducting ground. It is elementary to show that $\tilde{E}_\theta$ vanishes at $\theta = \pi/2$ in this case.

The integrals I_1 and I_2 can be evaluated in closed form. We obtain

$$I_1 = R(\theta)(\cot\theta - \csc\theta) - [\cot\theta + \csc\theta \, \text{sgn}(\theta - \theta_0)] \tag{17}$$

$$I_2 = -\sin\theta \left[\frac{\text{sgn}(\theta - \theta_0)}{(\cos\theta - \cos\theta_0)^2} + \frac{R(\theta)}{(\cos\theta + \cos\theta_0)^2} \right] \tag{18}$$

where $\text{sgn}(\cdot)$ is the signum function. The integral I_3 cannot be evaluated in closed form. It can, however, be evaluated numerically if kr_0 is not too large (say, less than 20, which corresponds to a frequency of approximately 18 MHz). For larger values of kr_0, asymptotic methods are appropriate. The details of the asymptotic evaluation of I_3 for $kr_0 >> 1$ are given in the Appendix. The result is

$$I_3 \sim \frac{-1}{\sqrt{2\pi j kr_0 \sin\theta \sin\theta_0}} \left\{ \frac{\sin(\theta - \theta_0)e^{jkr_0 \cos(\theta - \theta_0)}}{[1 - \cos(\theta - \theta_0)]^2} F_1 \right. \tag{19}$$

8

$$+\frac{jR(\theta)\sin(\theta-\theta_0)e^{-jkr_0\cos(\theta-\theta_0)}}{[1+\cos(\theta-\theta_0)]^2}\,F_2$$

$$+\frac{j\sin(\theta-\theta_0)e^{jkr_0\cos(\theta+\theta_0)}}{[1-\cos(\theta+\theta_0)]^2}\,F_3$$

$$+\left.\frac{R(\theta)\sin(\theta+\theta_0)e^{-jkr_0\cos(\theta+\theta_0)}}{[1+\cos(\theta+\theta_0)]^2}\,F_4\right\}$$

where

$$F_1 = \cot\theta\tan\left(\frac{\theta-\theta_0}{2}\right)S_0(jkr_0p_1) \tag{20}$$

$$+\left[1-\cot\theta\tan\left(\frac{\theta-\theta_0}{2}\right)\right]S_1(jkr_0p_1)$$

$$F_2 = \cot\theta\cot\left(\frac{\theta-\theta_0}{2}\right)S_0(jkr_0p_2) \tag{21}$$

$$+\left[1-\cot\theta\cot\left(\frac{\theta-\theta_0}{2}\right)\right]S_1(jkr_0p_2)$$

$$F_3 = \cot\theta\tan\left(\frac{\theta+\theta_0}{2}\right)S_0(jkr_0p_3) \tag{22}$$

$$+\left[1-\cot\theta\tan\left(\frac{\theta+\theta_0}{2}\right)\right]S_1(jkr_0p_3)$$

9

$$F_4 = \cot\theta \cot\left(\frac{\theta + \theta_0}{2}\right) S_0(jkr_0p_4) \tag{23}$$

$$+ \left[1 - \cot\theta \cot\left(\frac{\theta + \theta_0}{2}\right)\right] S_1(jkr_0p_4)$$

with

$$p_1 = 1 - \cos(\theta - \theta_0) \tag{24}$$

$$p_2 = 1 + \cos(\theta - \theta_0) \tag{25}$$

$$p_3 = 1 - \cos(\theta + \theta_0) \tag{26}$$

$$p_1 = 1 + \cos(\theta + \theta_0) \tag{27}$$

$$S_0(\xi) = \sqrt{\pi\xi}\, e^{\xi} \mathrm{erfc}\sqrt{\xi} \tag{28}$$

$$S_1(\xi) = \xi - \left(\xi - \frac{1}{2}\right) S_0(\xi) \tag{29}$$

and where erfc($\cdot$) denotes the complementary error function. It is not difficult to show that 1) the asymptotic representation for I_3 makes the electric field $\tilde{E}_\theta$ vanish at $\theta = \pi/2$ when the ground is not perfectly conducting; and 2) $\tilde{E}_\theta$ is well behaved at $\theta = \theta_0$, the singularity in I_3 at $\theta = \theta_0$ being cancelled by the singularity in I_2 at that angle.

This completes the evaluation of the radiated field in the frequency domain. It remains to determine the current at the feed point, $\tilde{I}_0(j\omega)$. This is done in the next section.
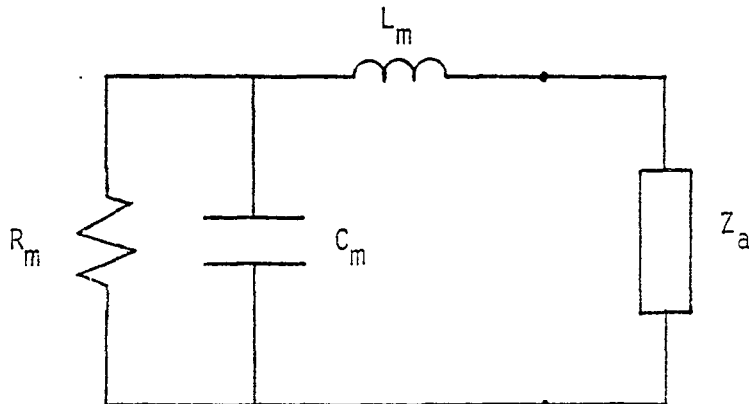
10

Figure 3: Equivalent-circuit model for the Marx generator and antenna. The voltage across C_m is V_0 at $t = 0$.

3 Antenna Feed Current

The Marx generator and antenna configuration is modeled by the equivalent circuit shown in Figure 3. The antenna impedance Z_a is given by [1]

$$Z_a = R_a + \frac{1}{j\omega C_a} \qquad (30)$$

where $R_a = 60$ ohms is the characteristic impedance of the biconical transmission line formed by the antenna and ground plane, and the antenna capacitance $C_a = 2.9$ nF. The capacitance C_m represents the erected Marx capacitance in parallel with the peaking capacitor; and $C_m = 5.4$ nF. The resistance R_m represents the charging resistors, the Marx triggering resistors, and the non-zero conductivity of the liquid dielectric in the peaking capacitor. The total resistance is approxi-

11

mately 3.7 kΩ [5]. The inductance L_m represents the total inductance of the Marx generator and limits the rise rate of the antenna current. We have chosen a value for L_m of 0.245 μH; this value yields a 10% - 90% rise time for the antenna current of 9 ns.

The antenna feed current $\tilde{I}_0(j\omega)$ is found from the equivalent circuit to be

$$\tilde{I}_0(j\omega) = \frac{j\omega\tau_m C_a V_0}{1 + j\omega\left\{\tau_a + \tau_m(1 + C_a/C_m) + j\omega\left[\tau_a\tau_m + (1 + j\omega\tau_m)/\omega_a^2\right]\right\}} \quad (31)$$

where $\tau_a = R_a C_a$, $\tau_m = R_m C_m$ and $\omega_a^2 = 1/(L_m C_a)$; V_0 is the pulser charge voltage. Eq. (31) may now be substituted in eq. (6) to yield the frequency-domain radiated electric field $\tilde{E}_\theta$.

A plot of the magnitude of $\tilde{I}_0(j\omega)/V_0$ as a function of frequency is shown in Figure 4. The break frequencies in the magnitude spectrum are approximately 5 kHz, 1.5 MHz, and 37 MHz. A plot of $I_0(t)/V_0$ as a function of time is shown in Figure 5. The current peaks at $t = 14$ ns and changes sign at $t = 460$ ns.

4 Representative Time-Domain Results

In this section we present numerical data for the radiated electric field. The ground surface around the VPD-II antenna is covered with a wire mesh, so we must account for its presence in calculating the reflection coefficient $R(\theta)$. We use an equivalent sheet-impedance model to describe the mesh [8]. It is simple to
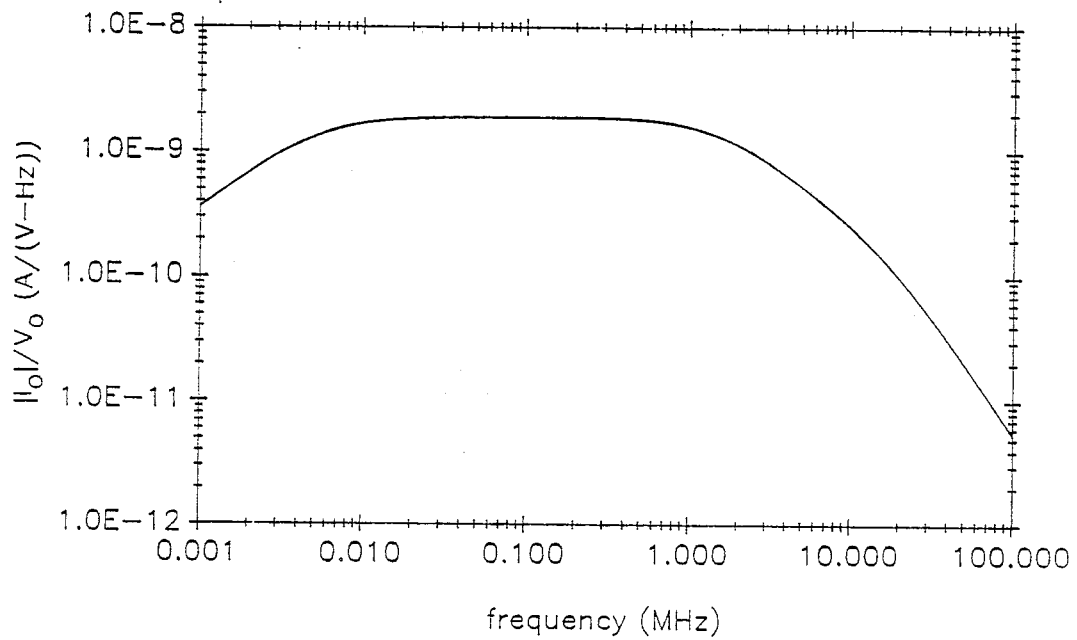
12

Figure 4: Magnitude of antenna current spectrum $| \tilde{I}_0(j\omega) |$ normalized to pulser voltage V_0 as a function of frequency.
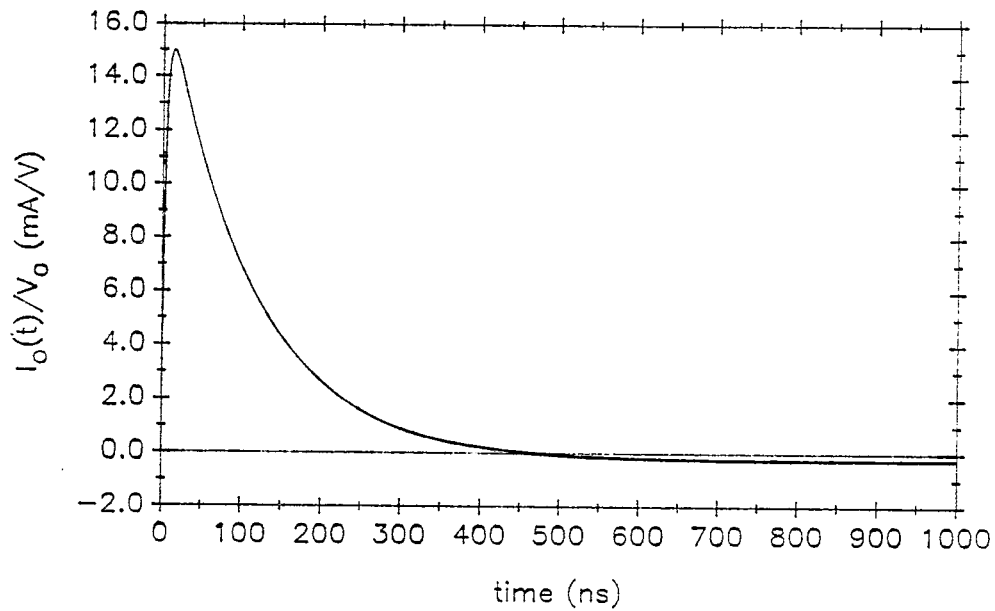

Figure 5: Antenna current $I_0(t)$ normalized to pulser voltage V_0.

13

show that $R(\theta)$ is given by

$$R(\theta) = \frac{Z_s\left(\hat{\epsilon}_r \cos\theta - \sqrt{\hat{\epsilon}_r - \sin^2\theta}\right) + Z_0 \cos\theta\sqrt{\hat{\epsilon}_r - \sin^2\theta}}{Z_s\left(\hat{\epsilon}_r \cos\theta + \sqrt{\hat{\epsilon}_r - \sin^2\theta}\right) + Z_0 \cos\theta\sqrt{\hat{\epsilon}_r - \sin^2\theta}} \qquad (32)$$

where $\hat{\epsilon}_r$ denotes the (complex) relative permittivity of the ground and Z_s is the equivalent sheet impedance of the mesh in the air-ground interface. For this field polarization, Z_s is given by

$$Z_s = Z_w' a_s + \frac{j\omega\mu_0 a_s}{2\pi} \ln(1 - e^{-2\pi r_w/a_s})^{-1}\left(1 - \frac{\sin^2\theta}{1 + \hat{\epsilon}_r}\right) \qquad (33)$$

where a_s is the mesh size (the meshes are assumed to be square) and r_w is the mesh-wire radius. Z_w' is the impedance per unit length of the mesh wire. The equivalent sheet-impedance model for the mesh is valid over the frequency range in which the individual meshes are electrically small. The mesh used for the ground plane at VPD-II has $a_s = 10$ cm and $r_w = 1.9$ mm.

The complex relative permittivity $\hat{\epsilon}_r$ is taken to be of the form developed by Messier [9]

$$\sqrt{\hat{\epsilon}_r} = \sqrt{\epsilon_{r\infty}} + \sqrt{\frac{\sigma_0}{j\omega\epsilon_0}} \qquad (34)$$

where $\epsilon_{r\infty}$ is the high-frequency relative permittivity of the ground and σ_0 is the low-frequency conductivity. We use $\epsilon_{r\infty} = 8$ (currently accepted as a "best" value for most soils) and $\sigma_0 = 3 \times 10^{-3}$ S m^{-1}, a value suitable for the vicinity of VPD-II.
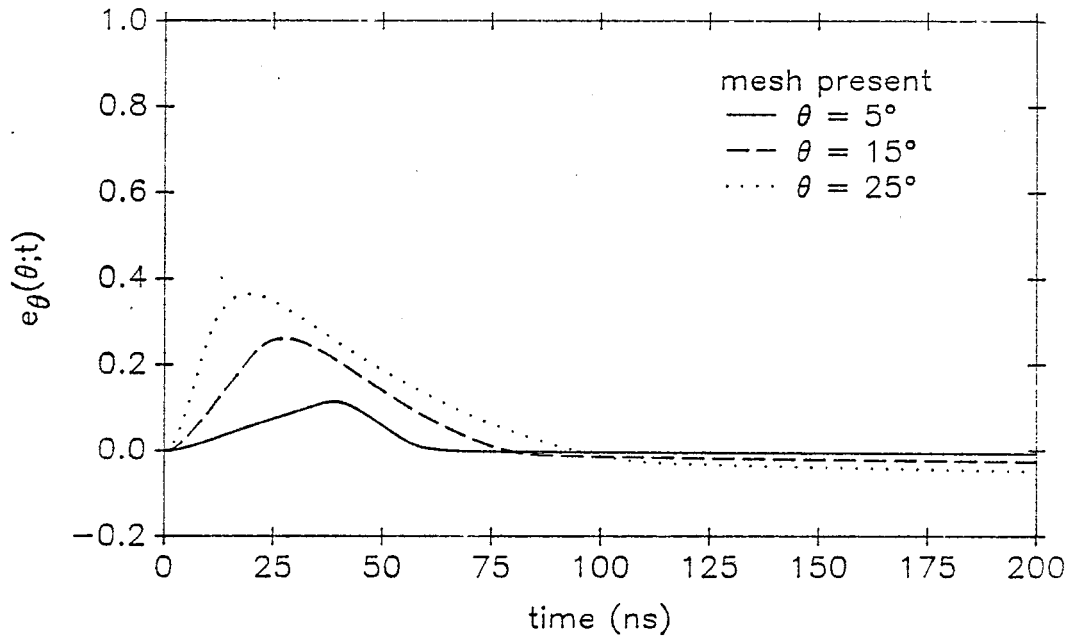
14

Figure 6: Normalized electric field $e_\theta(\theta; t)$; $\theta = 5°, 15°, 25°$; mesh present.

We have performed representative calculations of the normalized time-domain electric field e_θ, defined by

$$e_\theta(\theta; t) = \frac{rE_\theta(r, \theta; t - r/c)}{V_0} \tag{35}$$

The results are shown in Figures 6–8. One will observe that the peak amplitude and the rise rate of the field increase as the observation angle θ increases to approximately 65°, and remain nearly constant for θ up to approximately 85°. At larger observation angles, the rise rate and the peak value decrease, and the space-wave field vanishes at $\theta = 90°$. Most of the decrease takes place in the angular range $89° \le \theta \le 90°$. The space-wave field "holds up" to such large observation angles because of the efficacy of the mesh in establishing a ground plane.

In Figures 9–11 are shown plots of $e_\theta(\theta; t)$ vs. t for various values of θ, for the case in which the mesh is absent from the air-ground interface. The peak

15

amplitude and rise rate of the field again increase as the observation angle θ increases to approximately 65°, but then decrease rapidly, in comparison to the case in which the mesh is present, as θ is further increased. The peak amplitude reached near $\theta = 65°$ when the mesh is absent is about 75% of the peak amplitude attained when the mesh is present.

The mesh beneath the VPD-II antenna is actually of finite size and a more nearly complete analysis of the radiated field should take its size and shape into account. However, the radiated field would lie between the results presented here for the "mesh present" and "mesh absent" cases, depending on the observation angles θ and ϕ. In general, one would expect that if the observer location were such that the image of the antenna could be "seen" in the mesh ground plane, the "mesh present" results would better represent the radiated field. Otherwise, the "mesh absent" results would be more accurate.

In order to convert values of e_θ obtained from the calculations into estimates of field strength E_θ, one must know the range r and the charge voltage V_0. The pulser which drives the VPD-II antenna was originally designed to produce a peak output voltage greater than 5 MV, but because of the existence of breakdown problems in the output switch housing, the peak voltage obtainable is only about 4 MV. A typical value for V_0 to use in field calculations is 3.5 MV.
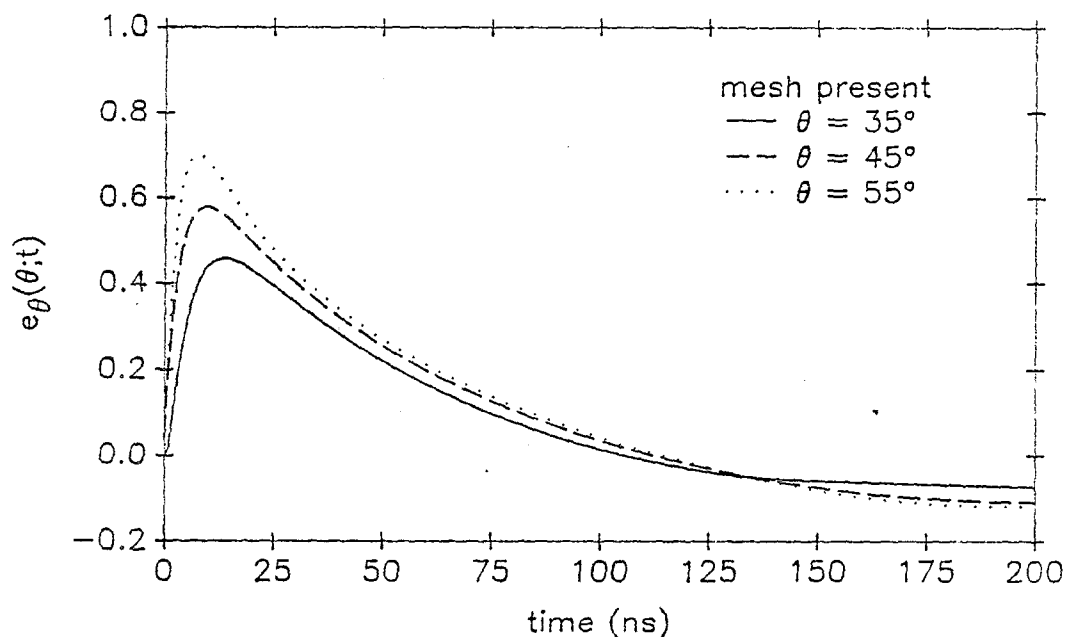
Figure 7: Normalized electric field $e_\theta(\theta; t); \theta = 35°, 45°, 55°$; mesh present.

5 Concluding Remarks

We have used a model for the surface current density on the VPD-II antenna to obtain the far-zone radiated electromagnetic field when the antenna is situated over an imperfectly conducting ground with or without a wire mesh in the air-ground interface. It is found that the rise rate and the peak amplitude of the radiated field increase as the observation angle increases from 0° (directly above the antenna) to around 65°. When the mesh is present, these quantities are nearly constant up to observation angles very close to 90°, where the space-wave field vanishes. The peak electric field intensity in the space-wave field is approximately $840\ V_{0M}/r_{km}$ volts per meter, where V_{0M} is the pulser charge voltage in MV and r_{km} is the range in kilometers. For a charge voltage of 3.5 MV, the peak electric field intensity is approximately 3 kV/m at a range of one kilometer for an observer
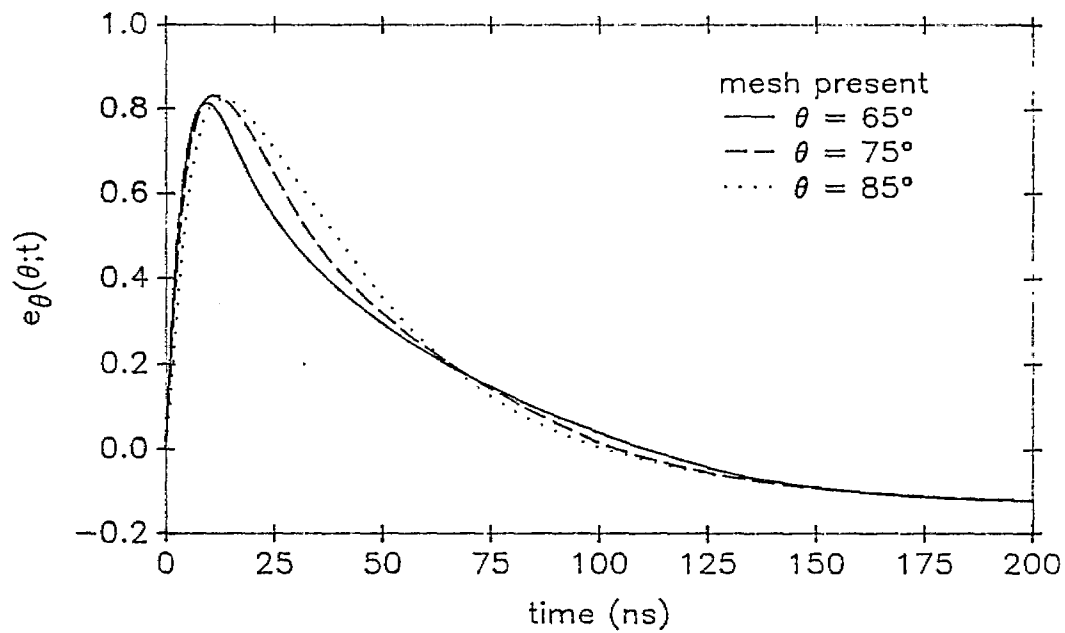
17

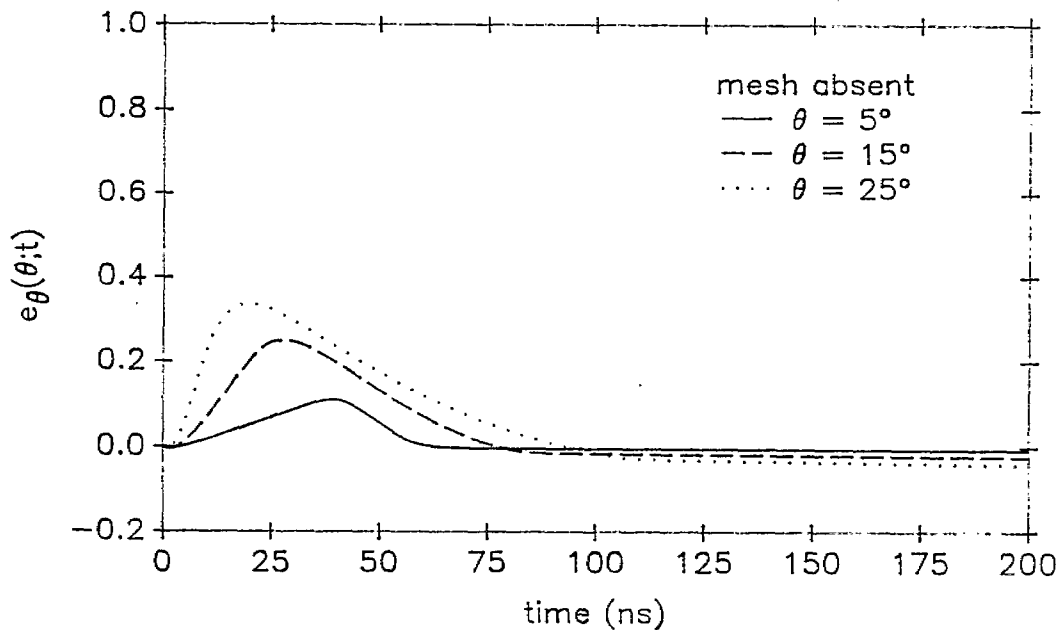Figure 8: Normalized electric field $e_\theta(8;t); \theta = 65°, 75°, 85°$; mesh present.

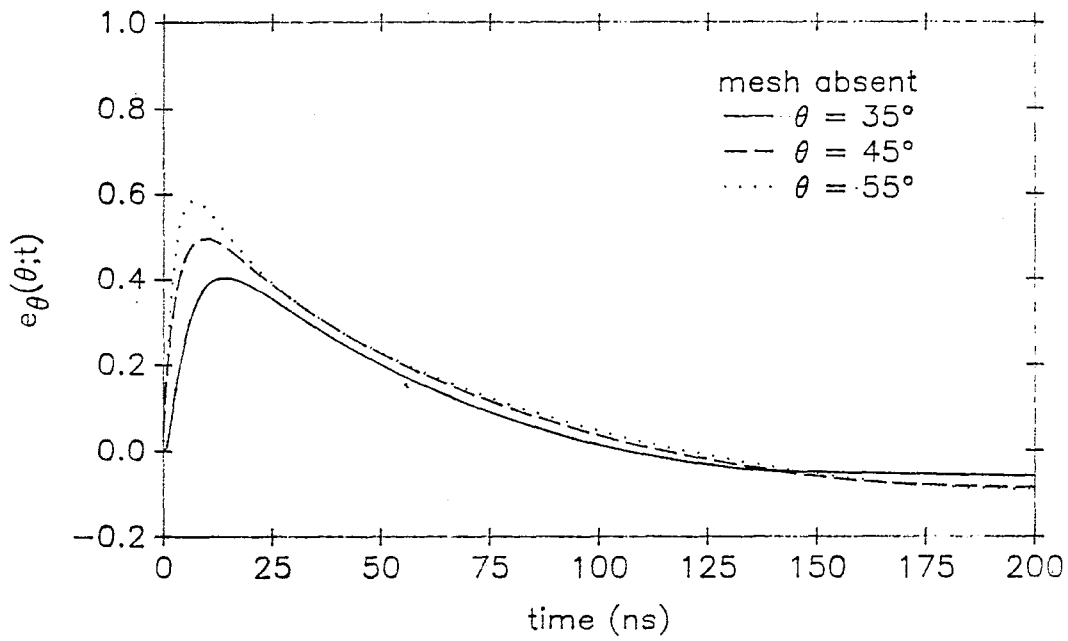Figure 9: Normalized electric field $e_\theta(\theta;t); \theta = 5°, 15°, 25°$; mesh absent.

18

Figure 10: Normalized electric field $e_\theta(\theta; t); \theta = 35°, 45°, 55°$; mesh absent.
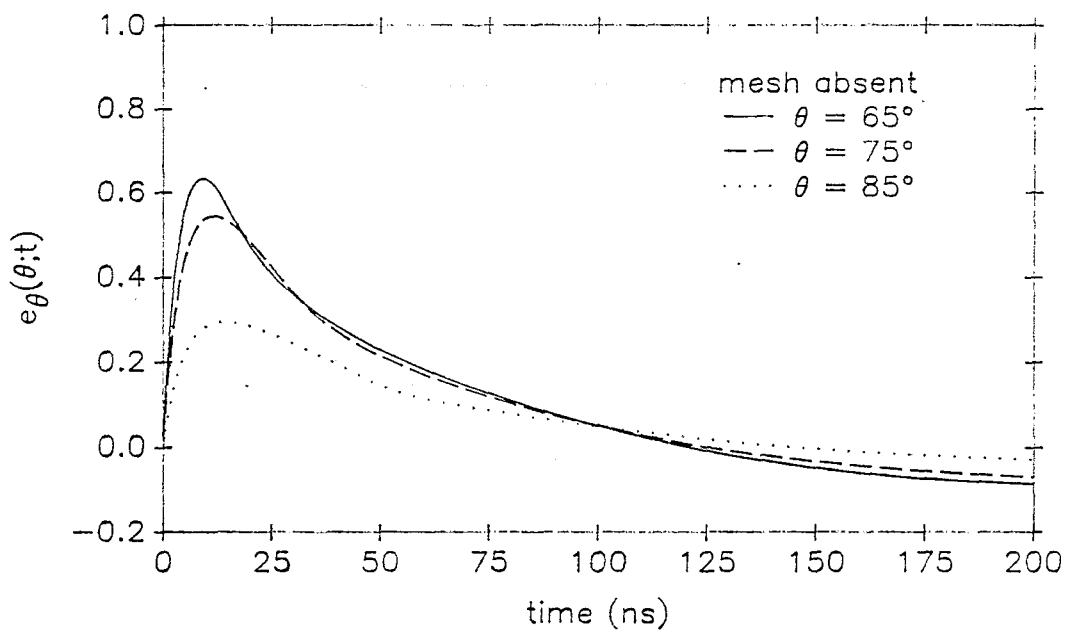

Figure 11: Normalized electric field $e_\theta(\theta; t); \theta = 65°, 75°, 85°$; mesh absent.

19

well above the air-ground interface.

When the mesh is absent, the rise rate and peak amplitude of the space-wave field begin to decrease, after reaching a maximum around $\theta = 65°$, much more rapidly with increases in θ than do these same quantities when the mesh is present. The peak intensity in the field when the mesh is absent is approximately 640 V_{0M}/r_{km} volts per meter. For a pulser charge voltage of 3.5 MV, the peak electric field intensity is approximately 2.25 kV/m at a range of one kilometer for an observer well above the air-earth interface.

Our treatment of this problem accounts only for the space-wave contribution to the total field. Since the ground is not perfectly conducting, this field contribution vanishes in the air-earth interface. The field at great distances from the antenna is dominated, for observers close to the air-ground interface, by the ground-wave contribution to the total field. This field contribution is considered in a separate note.

APPENDIX: Asymptotic Evaluation of I_3

Contributions to an integral of the form

$$I = \int_a^b e^{jkr_0 p(\phi')} q(\phi') d\phi' \tag{A1}$$

in the limit of large kr_0 can arise from the endpoints of the integration interval, from stationary points of the integrand, and from poles or other singularities. The integral I_3 is made up of two integrals having the form given in eq. (A1) with $p(\phi')$ and $q(\phi')$ periodic with period 2π and with $b-a = 2\pi$. The endpoint contributions thus cancel, and we consider contributions to the constituent integrals of I_3 from the stationary points ϕ_s where $p'(\phi_s) = 0$.

The contribution to an integral of the form given in eq. (A1) from a stationary point at $\phi' = \phi_s$ within the interval (a, b) is [10]

$$I \sim e^{jkr_0 p(\phi_s)} q(\phi_s) e^{\pm j\pi/4} \left| \frac{2\pi}{kr_0 p''(\phi_s)} \right|^{1/2} \quad (kr_0 \to \infty) \tag{A2}$$

where the upper or lower sign is taken as $p''(\phi_s)$ is positive or negative. Define

$$p(\phi') = \sin\theta \sin\theta_0 \cos\phi' \tag{A3}$$

$$q_\pm(\phi') = -\frac{(\pm\sin\theta\cos\theta_0 - \sin\theta_0\cos\theta\cos\phi')e^{\pm jkr_0\cos\theta\cos\theta_0}}{(1 \mp \cos\theta\cos\theta_0 - \sin\theta\sin\theta_0\cos\phi')^2} \tag{A4}$$

so that I_3 can be expressed as

$$I_3 = \frac{1}{2\pi} \int_{-\pi/2}^{3\pi/2} q_+(\phi') e^{jkr_0 p(\phi')} d\phi' - \frac{R(\theta)}{2\pi} \int_{-\pi/2}^{3\pi/2} q_-(\phi') e^{jkr_0 p(\phi')} d\phi' \tag{A5}$$

21

where we have set $\phi = 0$ and shifted the limits of integration without loss of generality. The stationary points of $p(\phi')$ are located at $\phi' = 0$ and $\phi' = \pi$ with

$$p(0) = \sin\theta \sin\theta_0 \tag{A6}$$

$$p''(0) = -\sin\theta \sin\theta_0 \tag{A7}$$

$$p(\pi) = -\sin\theta \sin\theta_0 \tag{A8}$$

$$p''(\pi) = \sin\theta \sin\theta_0 \tag{A9}$$

$$q_+(0) = \frac{-\sin(\theta - \theta_0)}{[1 - \cos(\theta - \theta_0)]^2} \, e^{jkr_0 \cos\theta \cos\theta_0} \tag{A10}$$

$$q_+(\pi) = \frac{-\sin(\theta + \theta_0)}{[1 - \cos(\theta + \theta_0)]^2} \, e^{jkr_0 \cos\theta \cos\theta_0} \tag{A11}$$

$$q_-(0) = \frac{\sin(\theta + \theta_0)}{[1 + \cos(\theta - \theta_0)]^2} \, e^{-jkr_0 \cos\theta \cos\theta_0} \tag{A12}$$

$$q_-(\pi) = \frac{\sin(\theta - \theta_0)}{[1 + \cos(\theta - \theta_0)]^2} \, e^{-jkr_0 \cos\theta \cos\theta_0} \tag{A13}$$

Substituting eqs. (A6) - (A13) into eqs. (A2) and (A5) as appropriate, we obtain the results for I_3 given in eq. (19) of the text, except for the factors F_i.

We observe that the contribution to I_3 which arises from the stationary point $\phi' = 0$ in the integral involving $q_+(\phi')$ is singular at $\theta = \theta_0$. The presence of this singular behavior, which is not cancelled by the singularity in I_2 at $\theta = \theta_0$, indicates that a more careful evaluation is needed. We employ a modified saddle-point method to evaluate that contribution to I_3.

22

We begin by expressing $\cos \phi'$ near the point $\phi' = 0$ as

$$\cos \phi' \cong 1 - \frac{1}{2}\phi'^2 \qquad (A14)$$

so that the integral is written as

$$I = -\frac{1}{2\pi}e^{jkr_0 \cos(\theta - \theta_0)} \int_{(0)} \frac{[\sin(\theta - \theta_0) + \frac{\phi'^2}{2} \sin\theta_0 \cos\theta]e^{-jkr_0 \sin\theta \sin\theta_0 \phi'^2/2}}{[1 - \cos(\theta - \theta_0) + \frac{\phi'^2}{2} \sin\theta \sin\theta_0]^2} \, d\phi' \qquad (A15)$$

where the integral is to be evaluated "near $\phi' = 0$". Next make the substitution

$$\phi' = \rho e^{-j\pi/4} \qquad (A16)$$

so that the exponential factor in the integrand becomes

$$e^{-jkr_0 \sin\theta \sin\theta_0 \phi'^2/2} = e^{-kr_0 \sin\theta \sin\theta_0 \rho^2/2} \qquad (A17)$$

and integration along real values of the variable ρ is equivalent to a steepest-descent integration. We recall that $0 \leq \theta \leq \pi/2$ and $0 \leq \theta_0 \leq \pi/2$, so that the exponent on the right-hand side of eq. (A17) is negative and real.

Now recognizing that the integrand is an even function of ρ, we have

$$I = -\frac{e^{-j\pi/4}}{\pi}e^{jkr_0 \cos(\theta - \theta_0)} \int_0^\infty \frac{[\sin(\theta - \theta_0) - j\frac{\rho^2}{2} \sin\theta_0 \cos\theta]}{[1 - \cos(\theta - \theta_0) - \frac{j\rho^2}{2} \sin\theta \sin\theta_0]^2} \cdot$$
$$e^{-kr_0 \sin\theta \sin\theta_0 \rho^2/2} d\rho \qquad (A18)$$

Change the integration variable to t, where

$$t = \frac{\rho^2}{2} \sin\theta \sin\theta_0 \qquad (A19)$$

23

and define

$$p = 1 - \cos(\theta - \theta_0) \qquad (A20)$$

so that

$$I = -\frac{e^{j\pi/4}e^{jkr_0\cos(\theta-\theta_0)}}{\pi\sqrt{2\sin\theta\sin\theta_0}} \int_0^\infty e^{-kr_0 t} G(t) \frac{dt}{\sqrt{t}} \qquad (A21)$$

where

$$G(t) = \frac{t\cot\theta + j\sin(\theta-\theta_0)}{(t+jp)^2} \qquad (A22)$$

We note that if t is set equal to zero in $G(t)$ and the integral in eq. (A21) evaluated, we recover the first term in eq. (19) of the text, except for the factor F_1.

Expand $G(t)$ in a Laurent series about $-jp$:

$$G(t) = \frac{j\sin(\theta-\theta_0) - jp\cot\theta}{(t+jp)^2} + \frac{\cot\theta}{t+jp} \qquad (A23)$$

yielding

$$I = -\frac{e^{j\pi/4}e^{jkr_0\cos(\theta-\theta_0)}}{\pi\sqrt{2\sin\theta\sin\theta_0}} \left\{ \cot\theta + [p\cot\theta - \sin(\theta-\theta_0)]\frac{d}{dp} \right\} \cdot$$

$$\int_0^\infty \frac{e^{-kr_0 t}dt}{\sqrt{t}(t+jp)} \qquad (A24)$$

This integral is known. We have [11]

$$\int_0^\infty \frac{e^{-kr_0 t}dt}{\sqrt{t}(t+jp)} = \frac{\pi}{\sqrt{jp}}e^{jkr_0 p}\operatorname{erfc}\sqrt{jkr_0 p} \qquad (A25)$$

where erfc($\cdot$) denotes the complementary error function. Performing the differentiation in eq. (A24) and using eq. (A25), we obtain, after a little algebra, the first term of eq. (19) in the text.

We remark that the function F_1 defined in eq. (20) approaches unity as $kr_0 \to \infty$ if $\theta - \theta_0 \neq 0$. It is also not difficult to show, using the series expansion for the error function, that the singular behavior near $\theta = \theta_0$ of the asymptotic representation for I_3 exactly cancels the singular behavior of I_2 (cf. eq. (18)) at that point. Thus the asymptotic representation for the radiated field is well behaved near $\theta = \theta_0$.

Each of the integrals I_1, I_2, and I_3 vanishes at $\theta = \pi/2$ for an imperfectly-conducting ground. The same is true for the asymptotic representation of I_3 developed from a stationary-phase analysis at the beginning of this Appendix. The more refined analysis, however, yields correction terms in the function F_1 which are not cancelled by corresponding terms in the stationary-phase contribution from $q_-(0)$. In order to correct this minor defect and to obtain a consistent asymptotic representation for I_3, we simply perform the more refined analysis on each of the remaining contributions to I_3. The result is given in eq. (19) of the text.

References

[1] Carl E. Baum, "Resistively Loaded Radiating Dipole Based on a Transmission-Line Model for the Antenna", *Sensor and Simulation Notes*, Note 81, April 1969.

[2] W. S. Kehrer and C. E. Baum, "Electromagnetic Design Parameters for ATHAMAS II (VPD-II), *ATHAMAS Memos*, Memo 4, May 1975.

[3] B. K. Singaraju, C. E. Baum, and J. H. Darrah, "Design Improvements Incorporated in Athamas II (Larger VPD)", *ATHAMAS Memos*, Memo 11, January 1976.

[4] B. K. Singaraju, C. E. Baum, J. H. Darrah, and D. Rossbach, "Use of ATHAMAS II (Larger VPD) for Testing Aircraft in Flight", *ATHAMAS Memos*, Memo 12, April 1976.

[5] J. C. Giles, J. C. Leib, and G. D. Sower, "Field Mapping Data for ATHAMAS-II", *ATHAMAS Memos*, Memo 23, March 1979.

[6] D. R. Wilton, "Static Analysis of [a] Conical Antenna Over a Ground Plane", *Sensor and Simulation Notes*, Note 224, August 1976.

[7] D. R. Wilton, "Dynamic Analysis of a Loaded Conical Antenna Over a Ground Plane", *Sensor and Simulation Notes*, Note 225, August 1976.

[8] K. F. Casey, "EMP Penetration Through Advanced Composite Skin Panels", *Interaction Notes*, Note 315, December 1976.

[9] M. A. Messier, "The Propagation of an Electromagnetic Impulse through Soil: Influence of Frequency-Dependent Parameters", Mission Research Corporation Report No. MRC-N-415, 1980.

[10] F. W. J. Olver, *Asymptotics and Special Functions*, Academic Press, New York, 1974, p. 97.

[11] M. Abramowitz and I.A. Stegun, eds., *Handbook of Mathematical Functions*, AMS-55, National Bureau of Standards, no. 7.4.9, p. 302.